Visualizing strongly-correlated electrons with a novel scanning tunneling microscope

Battisti, I.

3

Dome: design and construction of an ultra-stable scanning tunneling microscope

This chapter has been published as:
Battisti *et al.*, Rev. Sci. Instrum. **89**, 123705 (2018).

3.1 Introduction

This chapter describes the design, construction and performance of our fully home-built scanning tunneling microscope optimized for spectroscopic-imaging measurements, that we called *Dome*. Chapter 2 gives an introduction to the working principle of STM and to the different types of measurements that can be performed, but does not discuss technical challenges. For instance, how is it possible to bring and keep two macroscopic objects such as tip and sample at a constant distance of few angstroms from each other? And more generally, what are the most critical points one has to take care of when designing and building a microscope?

Here, we start in section 3.1.1 by describing the factors that most critically affect STM measurements and, in light of that, we give an overview of the key specifications for designing an STM dedicated to spectroscopic-imaging. We then explain some basic principles of vibration isolation in section 3.1.2, to motivate the choices we made for the design of Dome. In the remainder of the chapter, we discuss the design, construction and performance of the microscope, which is shown in Fig. 3.1 as a computer-aided design (CAD) rendering. We start in section 3.2 with the STM head where tip and sample are placed, therefore the most critical part of the instrument. We show how finite element analysis calculations guide our design choices to obtain a very stiff microscope. Combined with a careful choice of materials, this leads to an STM head that is three times stiffer than what has been previously reported [52]. We continue with a description of the cryogenic insert (Sec. 3.3), the vibration isolation table (Sec. 3.4) and the UHV chamber (Sec. 3.5). Finally, we demonstrate the performance of the microscope by showing vibrational noise spectra and quasiparticle interference data on the correlated metal Sr_2RhO_4 (Sec. 3.6).

All data presented in chapter 2, 3 and 6 of this thesis is acquired with this new microscope.

3.1.1 The technical challenge of building an STM

The exponential dependence of the tunneling current on the tip-sample distance can be considered the main strength of STM, because it is the factor allowing it to resolve atoms. It is however also a considerable drawback: the smallest vibrations coupling to the tip-sample junction from the environment are directly transmitted, exponentially, to the tunneling current signal. And vibrations are, indeed, the main source of noise in STM measurements. When acquiring a topograph, the tip scans over the sample using a feedback mechanism that can partially correct for vibrations transmitted to the junction, as explained in chapter 2. During most spectroscopy experiments, instead, the feedback to the tip is switched off, and even the smallest vibration can

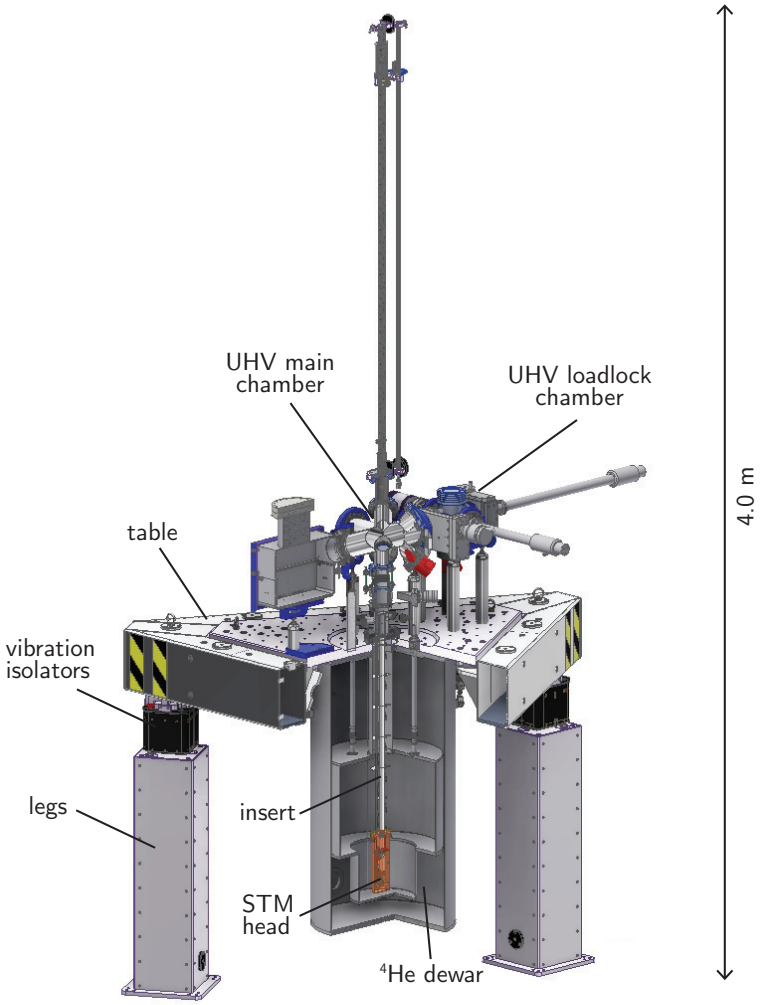

Figure 3.1: Overview of the full Dome microscope. The insert and the STM head are shown by virtually cutting open the CAD rendering. The most significant parts are indicated.

exponentially couple to the tunneling current, causing the $\mathrm{d}I/\mathrm{d}V$ spectra to be significantly noisier. For a spectroscopic map, typically $10^4 - 10^5$ spectra are acquired subsequently over a period of several days (up to a full week of continuous measurement). An extreme stability of the microscope against external vibrations is thus the prime requirement one has to meet when building an STM for spectroscopic imaging.

The other requirements depend on the samples and the physics one wants to study: low temperatures are needed for quantum materials and to achieve higher energy resolution, as explained in section 2.5; ultra high vacuum (UHV) is necessary to

prepare and maintain atomically clean surfaces; a magnet opens the possibility to study samples in a magnetic field.

Our instrument is designed to operate in UHV and at low temperatures, with an achieved base pressure $p = 3 \times 10^{-10}$ mbar and base temperature $T = 4.27$ K. Both low temperatures and UHV requirements make the building more challenging: only a selected amount of materials are compatible with cryogenic and UHV conditions. Moreover, one has to compensate for the different thermal contractions of different materials and to ensure good thermal stability to avoid thermal drift during cool down procedures and measurements.

3.1.2 Reducing vibrations in STM

The transmission of vibrations to the tunneling junction is typically reduced by combining a very rigid microscope construction with the use of a vibration isolation table (and, if available, laboratories with low-vibration facilities). In this section, we show that the reasons underlying this choice can be easily understood by considering both STM head and vibration isolation table as one-dimensional driven harmonic oscillators [29].

The basics of the isolation of a mass m from the vibrations of a reference frame can be understood as follows. Vibrations from the environment cause a time-dependent displacement of the reference frame $X(t)$ that, in turn, causes a displacement $x(t)$ of the mass m, as illustrated in the inset of Fig. 3.2a. We can simplify the induced displacement to a harmonic excitation of frequency ω by using Fourier decomposition. The mass then moves with the same frequency ω as the reference frame, with a phase difference ϕ:

$$\begin{aligned} X(t) &= X_0 \cos(\omega t), \\ x(t) &= x_0 \cos(\omega t - \phi). \end{aligned} \tag{3.1}$$

The equation of motion for the mass m contains the restoring force of the spring, with spring coefficient k, and a damping term, with damping coefficient ν:

$$m\ddot{x} = -k(x - X) - \nu(\dot{x} - \dot{X}). \tag{3.2}$$

It is useful to define the natural frequency of the system by $\omega_0 = 2\pi f_0 = \sqrt{k/m}$, and the damping term by $\gamma = \nu/2m$. One can then solve the equation of motion Eq. (3.2) by using the ansatz of Eq. (3.1), to obtain the expressions for the transfer function $\Gamma(\omega)$ and the phase difference $\phi(\omega)$, plotted in Fig. 3.2a-b, respectively:

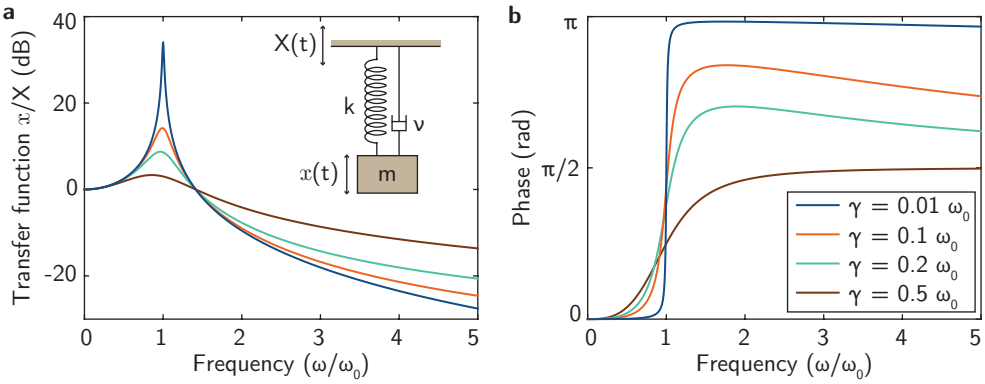

Figure 3.2: **a**, Transfer function of a harmonic oscillator with driven reference frame and damping, from Eq. (3.3). The system is schematically represented in the inset. **b**, Phase between the motion of m and the reference frame, from Eq. (3.4). Both transfer function and phase are shown for different damping values γ.

$$\Gamma(\omega) = \frac{x_0}{X_0} = \sqrt{\frac{\omega_0^4 + 4\gamma^2\omega^2}{(\omega_0^2 - \omega^2)^2 + 4\gamma^2\omega^2}}\,, \tag{3.3}$$

$$\phi(\omega) = \tan^{-1}\left(\frac{2\gamma\omega^3}{\omega_0^2(\omega_0^2 - \omega^2) + 4\gamma^2\omega^2}\right). \tag{3.4}$$

The problem of vibration isolation is to reduce the transfer function at all frequencies, while trying to push the resonance to a frequency where it is harming the least. Note that higher damping γ reduces the resonance peak height, but worsens the efficiency of vibration isolation for $\omega \gg \omega_0$ (see Fig. 3.2a). It is, therefore, necessary to find a compromise between reducing the peak height and having better isolation at higher frequency.

In an STM, typically one can find two systems that resemble such a harmonic oscillator. The first one is the vibration isolation table, with the table acting as the mass that is decoupled from the vibrating floor by means of (typically commercial) springs. Their natural frequency, $f_{\mathrm{iso}} = \omega_{\mathrm{iso}}/2\pi$, should be as low as possible, in order to have vibrations at most frequencies falling on the right-hand side of the resonance peak, where the transfer function is small (Fig. 3.2a). The second system resembling a harmonic oscillator is the STM head, with the sample as the reference frame, the tip as the mass, and the STM head connecting the two as the spring. In this case, one wants to avoid relative displacement between tip and sample, and this is achieved by having a very high value of the natural frequency $f_0 = \omega_0/2\pi$ for the STM head. One would then have most vibrations coupling on the far left-end side of the resonance peak, where the displacement is in phase, meaning that tip and sample will not move

relative to each other. In a continuous system such as the STM head, f_0 corresponds to the frequency of its first vibrational eigenmode, and it is directly related to the stiffness.

But what are the numbers in a real setup? The most damaging vibrations for STM measurements are in the 0−100 Hz range, introduced by people walking in the building, resonances of the building, and traffic (0−10 Hz), and by air ventilation and other appliances (10−100 Hz).

The vibration isolators of the table typically have a natural frequency f_{iso} of a few hertz (from 1-2 Hz for compressed air isolators, down to 0.5 Hz for negative spring coefficient isolators). The vibration isolation can be improved further by having a multiple stage system, where the STM table is placed on a heavy concrete block that is, in turn, resting on springs. This lowers f_{iso} further, however there is a lower limit at about 0.1 Hz.

The most room for improvement lies in the value of f_0 for the STM head. Typically, f_0 lies in the 1−5 kHz range, but can be increased of about one order of magnitude by choosing a smart design and stiff materials [29, 52], as we will show in the following. Obtaining a very stiff STM head, with the highest possible f_0, is, indeed, our main focus during the design phase.

3.2 The STM head

The STM head is often the most critical part in the determination of the microscope's performance. It needs to both guarantee a very stiff tip-to-sample connection and to provide an approach mechanism that allows to bring the tip from few millimeters away from the sample to tunneling distance. A beautiful solution to this problem was found 20 years ago by Pan et al. [53], with a design that is to date the best one for a cryogenic STM head. The stiffest cryogenic-compatible STM head that is reported in literature to date is based on this design, using oriented single-crystalline sapphire as the material for the body of the STM head [52]. This is our starting point. To improve the stiffness further, we optimize the geometry of all the components of the head with finite element analysis (FEA) calculations, towards achieving a higher f_0 of the fully assembled STM head.

Before describing the STM head design, we want to emphasize why sapphire is the ideal material from which to machine an STM head. Before White el al. (Ref. [52]) introduced sapphire as the main building material, the materials that have been used for STM heads are Macor or metals like titanium or molybdenum, mostly because they are much easier to machine. We note that is generally preferable to machine the STM head from an insulating material, to avoid the risk of electrical shorts. From

Material	ρ [g/cm^3]	E [GPa]	ν [-]	κ (4K) [W/m/K]
sapphire (Al_2O_3 99.99%)	3.98	360 - 440	0.32	100
Macor	2.52	66.9	0.29	0.1
titanium	4.54	110.3	0.32	0.1
molybdenum	10.22	330	0.32	60

Table 3.1: Properties of materials typically used for STM heads. Density ρ, Young's modulus E and Poisson's ratio ν are the structural properties defining the stiffness of the material. The thermal conductivity at low temperatures κ gives an indication for the thermalization times. The structural properties of sapphire and Macor are from Ref. [55]. The thermal properties at low temperatures are extracted from tables of Ref. [54] for sapphire, of Ref. [56] for Macor, and from Ref. [57] for the metals.

a quick look at the material properties in Table 3.1, it is clear that sapphire has the advantage of being stiffer, with a Young's modulus[1] much higher than Macor. Moreover, sapphire has an exceptionally high thermal conductivity at low temperatures, which is comparable to the one of copper and greatly exceeding the one of any other insulating material[2]. The main drawback of sapphire is that the material is very difficult to machine and prone to cracks. Recent advancements in production technology, however, allowed us to machine more complicated and detailed sapphire parts for the STM head than it was previously possible.

3.2.1 STM head design

The assembled STM head is shown in Fig. 3.3, in both CAD rendering and photographs.

Its main body is a hollow sapphire cylinder open on one side, inside which a triangular polished sapphire prism (the slider) is clamped via six shear piezo stacks[3] and a molybdenum plate acting as spring. The piezo stacks are glued with non-conductive epoxy[4] to the sapphire body, while the triangular prism is just clamped, and can

[1] The Young's modulus defines the relationship between stress and strain, and it is the mechanical property that measures the stiffness of a solid material.

[2] This is due to the extreme purity of single crystalline sapphire: heat in electrical insulators is carried only by phonons, and at low temperatures phonons are scattered only by defects and crystal boundaries, which are very rare in sapphire [54].

[3] P-121.01T from PI Ceramics, customized with height 2.7 mm, and polished Al_2O_3 end plates.

[4] Epotek H74F.

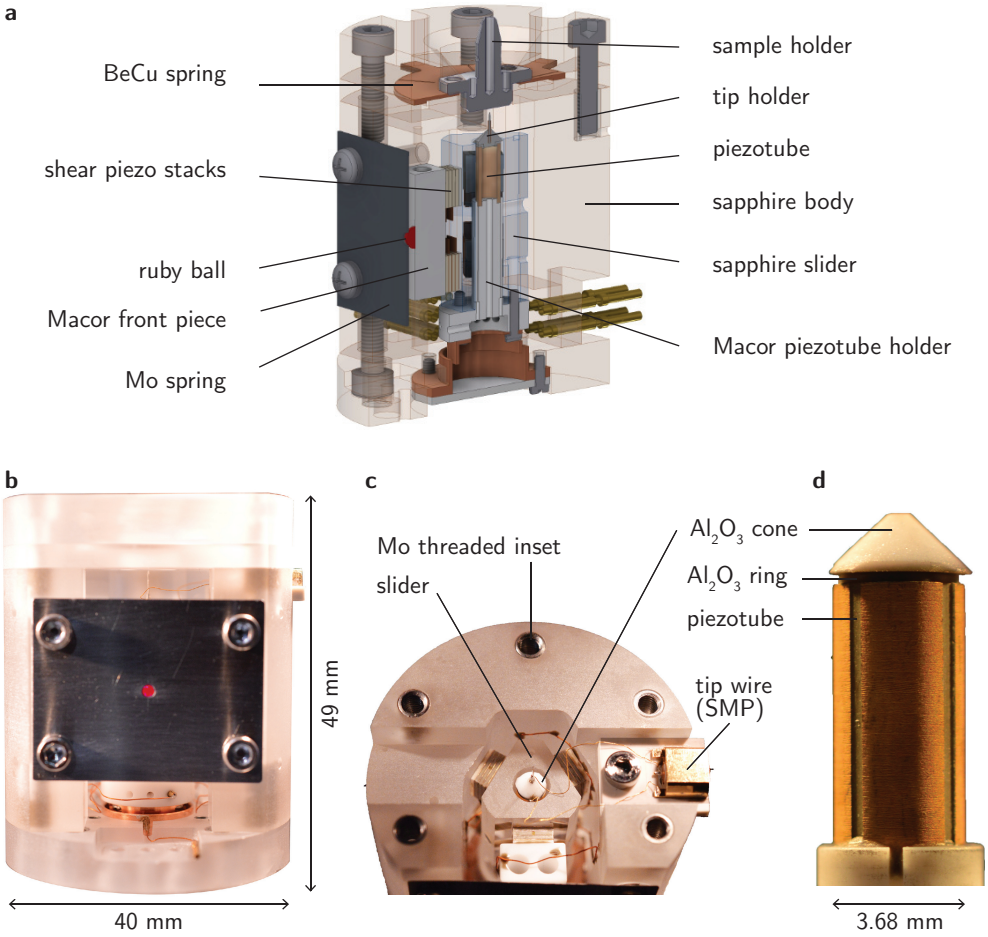

Figure 3.3: **a**, Cross section of the 3D CAD rendering of the STM head, with the main components being pointed out. **b**, Photograph of the fully assembled STM head. **c**, Top view of the open STM head, showing the slider construction and the tip holder. **d**, Photograph of the piezotube and tip holder during the construction phase.

slide up and down with respect to the body when high voltage pulses are applied to the piezo stacks (principle of stick-slip motion [29, 53]). This whole construction provides the coarse approach mechanism, also called *walker*, that allows to move the tip towards the sample over a 5 mm range with nanometer-sized steps (at 4 K, with 120 V pulses, one step up is about 20 nm). It is essential to the functioning of the walker to have very flat and perfectly parallel surfaces at the contact between the slider and the piezostacks, which requires polishing of the contacting surfaces.

The scanning motion is provided by a piezotube[5], which has four outer electrical contacts for deflections in the ±X, ±Y directions (in-plane) and one inner contact for contractions and elongation in Z. It is driven with maximum ±100 V on all contacts, resulting at 4 K in a XY field of view of 380 nm^2 and a Z elongation of 110 nm. The piezotube is glued with non-conductive epoxy on top of a Macor support which is in turn fixed inside the sapphire prism with screws.

The tip is mounted on a tip holder glued on top of the piezotube. The tip holder assembly is optimized for low weight, in order to increase the resonant frequencies of the scanner, and for low capacitance, in order to allow for high frequency STM measurements [58, 59]. It consists of a small Al_2O_3 ring glued directly on the piezotube, and a conical Al_2O_3 holder glued on the ring. This last piece hosts a small molybdenum cylinder inside which the tip is clamped by friction. The bottom surface of the conical piece is additionally sputtered with 450 nm of gold to provide a ground shield for the tip wire. With this assembly we obtain a tip-to-sample capacitance of 180 fF (at tunneling distance, with tip retracted) and a tip-to-ground shield capacitance of 2 pF. The tip-to-ground shield capacitance should be as low as possible to facilitate high frequency STM measurements, and the value we measure is reduced of more than a factor 10 with respect to commercially available instruments.

The sample holder receptacle is on top of the main body, with the sample facing downwards towards the tip and clamped by a BeCu spring. The scanner is not provided with an XY stage for coarse motion of the sample holder, in order to not reduce the stability of the assembly.

3.2.2 Improving the geometry with finite element analysis

The main factor allowing us to obtain a stiffer STM head is the optimization of the geometry, which we achieve by performing finite element analysis (FEA) calculations with the software package Comsol [60]. FEA calculations have been used before to improve the geometry of various scanning probe techniques [61–64], and in particular of high-scanning-speed STM [65–67], where high resonance frequencies are essential. Here, we use them for the first time to improve the geometry of a low-temperature STM for spectroscopic imaging.

The optimization procedure that we applied to several components of the STM head in order to achieve high resonant frequencies is shown in Fig. 3.4a. As an example, we discuss here how we apply this procedure to the piezotube. After importing the initial design in Comsol, we compute the mechanical eigenfrequencies of the first vibrational modes with the base of the piezotube fixed, as shown in Fig. 3.4b. We can identify two double degenerate bending modes, a rotational mode and a vertical mode. We then

[5] EBL4 from EBL Products. Height 8.0 mm, OD 3.68 mm, wall thickness 0.58 mm.

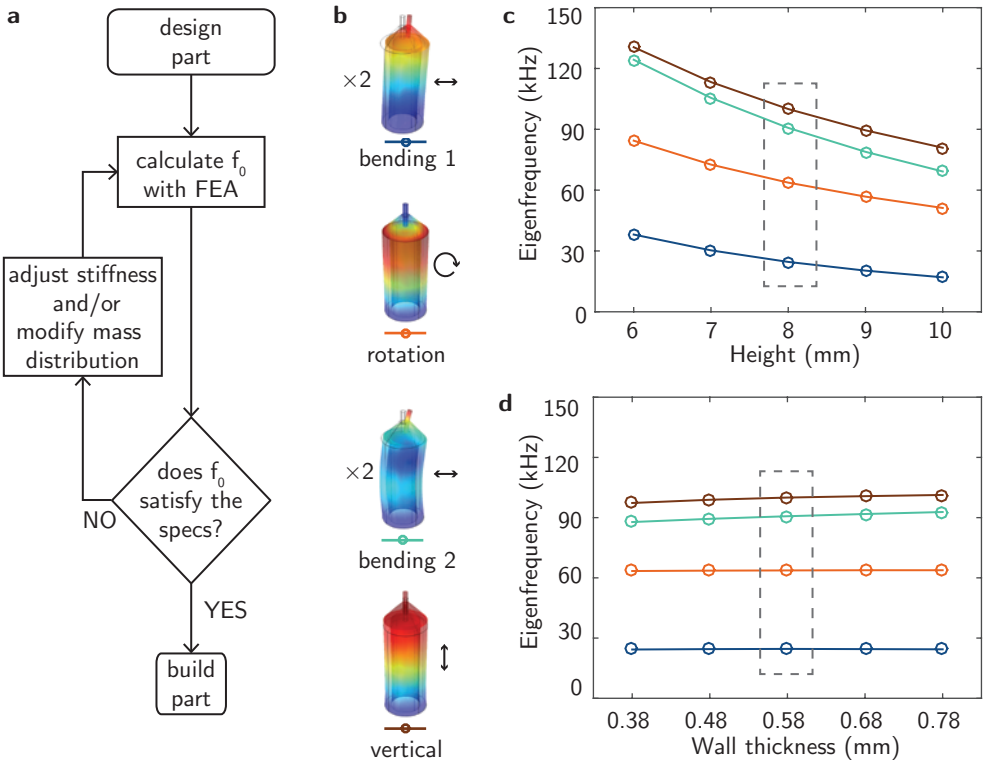

Figure 3.4: **a**, Flow chart explaining the procedure applied to several components of the STM head in order to achieve higher resonant frequencies. **b**, Mode shapes of the first six mechanical resonances of the piezotube as computed with Comsol, as a legend for panels **c**-**d**. The modes are shown as (exaggerated) displacements with colors from red (max displacement) to blue (no displacement). **c**, Variation of eigenfrequencies of the piezotube's modes with respect to the piezotube height, with base diameter fixed. **d**, Variation of eigenfrequencies of the piezotube's modes with respect to the wall thickness (with fixed outer diameter D=3.68 mm). The dashed boxes indicate the eigenfrequencies for the final chosen dimensions.

progressively change the dimensions of the part and recompute the eigenfrequencies, in order to understand which dimensions can be optimized to increase the stability. We find that is beneficial to lower the height (Fig. 3.4c), while changing the wall thickness (with fixed outer diameter) does not have a significant effect (Fig. 3.4d). In the case of a simple tube, this problem could also be solved analytically; however, here we want to show the procedure that then we will apply to more complicated parts of the STM head. In general, the optimization towards higher resonant frequencies can be limited by functional requirements and geometrical constraints. For the piezotube, reducing the aspect ratio between height and diameter diminishes the XY scanning

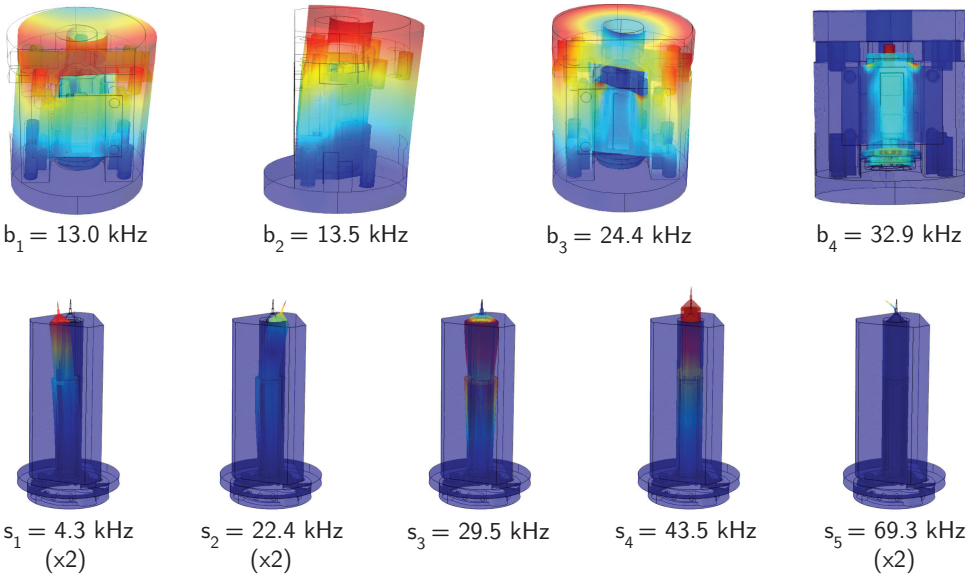

Figure 3.5: Main vibrational modes of the STM head, as calculated with Comsol, with the base of the STM fixed. The modes are shown as (exaggerated) displacements with colors from red (max displacement) to blue (no displacement). All the modes shown are calculated for the full design, but to ease visualization, the modes that belong to the scanner assembly (s_1-s_5) are shown separately. See the main text, Sec. 3.2.2, for a description of the modes.

range, and our final design is chosen as a compromise between stability and desired XY scanning range of $\approx 400\,\text{nm}$ at 4 K.

A similar analysis is performed on other STM head components, including the sapphire slider, the STM body, the Macor front piece and the sample holder. For instance, the simulations indicate that to reach a higher f_0, the STM head will benefit from a lower aspect ratio, a shorter and lighter sapphire slider and a lighter Macor front piece. The simulations also help determining until which point removing mass, for instance by drilling holes in the Macor front piece or in the sample holder, would help and when instead it would start hinder the stiffness of the part.

Finally, we also performed FEA calculations on the whole assembly of the STM head, simplified by removing small details in the design to allow for a simpler finite element mesh. This can provide further insights about the design choices, and moreover it can be directly compared to the measured values of the eigenfrequencies. The most significant modes that we obtain from FEA calculations of the full STM head are shown in Fig. 3.5. They can be divided in two groups: the modes belonging to the body of the STM ($b-$modes in Fig. 3.5) and the modes belonging to the scanner assembly ($s-$modes). The modes b_1, b_2 are almost degenerate and correspond to the

bending modes of the full head, b_3 corresponds to the rotational mode and b_4 to the motion of the slider inside the head. The modes s_1 and s_2 are double degenerate and correspond to first order and second order bending mode of the scanner, s_3 is the rotational mode of the scanner, s_4 the vertical mode of the scanner and s_5 is the bending mode of the tip.

Intuitively, one could think that the walker assembly used for coarse approach is the weakest point of the STM head design, and therefore that the lowest vibrational mode should correspond to the vertical motion of the slider inside the scanner (b_4). In our simulations, however, the main body vibrational modes and the scanner bending modes have lower frequencies, showing that the limiting factor for f_0 is mainly the STM head geometry. Clearly, the calculated value of the mode b_4 depends strongly on the stiffness of the shear piezo stacks that we feed into the simulation. The value of b_4 shown in Fig. 3.5 is obtained with half the stiffness reported in the specifications, to take into account the effect of glue and other factors involved in the mounting. Furthermore, the measured resonant frequencies reported in section 3.2.3 confirm that the slider construction is not the weakest point of the design.

3.2.3 Measurement of resonant frequencies

After the construction of the STM head, we measure both the eigenfrequencies of the walker assembly and of the piezotube assembly independently and we compare them with the calculations. The measurement is performed *in situ* with the head mounted in the cryogenic insert at room temperature and under vacuum. A lock-in amplifier is used to excite the piezo elements and to read out their response. The applied excitation is a sinusoidal signal of amplitude $1\,V_{\mathrm{peak-peak}}$ and sweeping frequency. A scheme of the circuit is presented in the inset of Fig. 3.6a [65]. Thanks to the intrinsic properties of piezoelectric materials, the electrical excitations V_{in} provided by the lock-in is converted into a mechanical excitation. When the excitation frequency corresponds to one of the STM eigenfrequencies, its amplitude gets enhanced, resulting in an enhanced electrical signal from the piezos V_{out} that is detected by the lock-in [65, 66].

Figure 3.6a-b show the transfer function obtained when exciting the six shear piezo stacks for the coarse approach connected in parallel. The main result is that we do not observe any resonant mode of the coarse approach assembly before 10 kHz, with the first strong peaks appearing at ≈13 kHz. We also performed the measurement at 4 K (not reported here), leading to slightly higher resonance frequencies due to the different stiffness of the materials at low temperatures and to thermal contractions. Remarkably, the value we achieve is a factor three better than the previously reported eigenfrequencies for a sapphire STM head [52], where the first strong peak in the coarse approach excitation appears at 4.6 kHz.

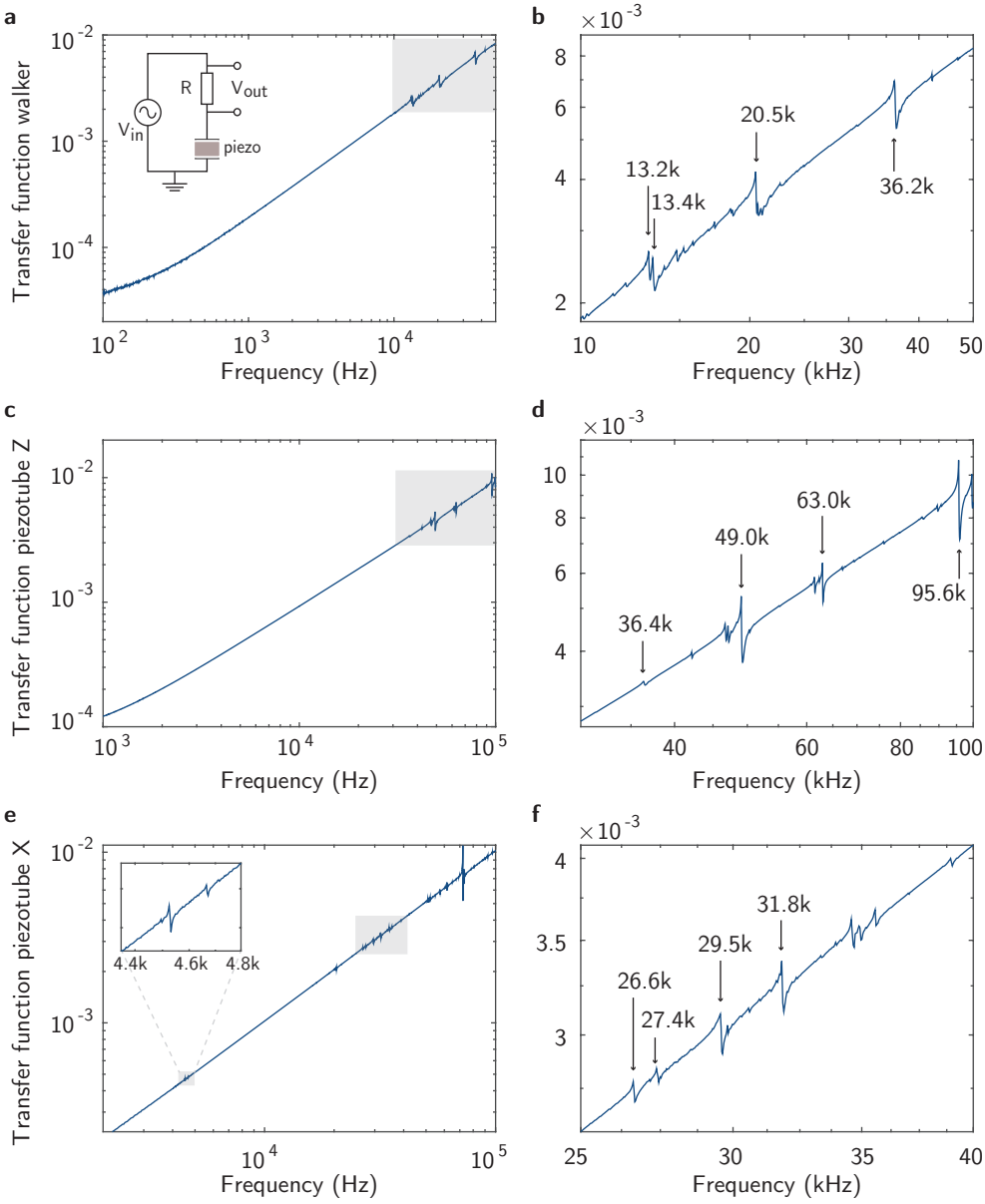

Figure 3.6: **a**, Measured transfer function V_{out}/V_{in} of the walker mechanism for the coarse approach. A scheme of the electronic circuit is shown in the inset, where R=11 Ω. **b**, Zoom of the gray area in **a**. **c**, Measured transfer function V_{out}/V_{in} of the piezotube vertical excitation. **d**, Zoom of the gray area in **c**. **e**, Measured transfer function V_{out}/V_{in} of the piezotube horizontal bending excitation. In the inset, a zoom of the low frequency peaks. **f**, Zoom of the gray area in **e**.

Additionally, we can now compare the measured resonances with the computed ones. We can easily identify the first two almost degenerate peaks at 13.2 kHz and 13.4 kHz as the two bending modes of the STM body (b_1, b_2). The peak at 20.5 kHz is more difficult to identify, but it could correspond to the rotational mode b_3. We interpret the peak measured at 36.2 kHz as the mode b_4, given that in the FEA calculations b_4 is the only mode we find in the frequency window between 30 kHz and 50 kHz, and in the measurement we do not observe any other peak before ≈80 kHz.

For the piezotube, we can measure the transfer function while exciting either the vertical modes (which are the most crucial ones) or the bending modes (which have less influence on the noise), simply by applying the excitation to different electrodes. In Fig. 3.6c-d we show the transfer function of the vertical modes, measured with the outer electrical contacts (±X,±Y) connected in parallel against the inner contact (Z) acting as ground. The small peak at 36.4 kHz results from coupling to the mode b_4, and the peak at 49.5 kHz can be identified as the vertical mode s_4 of the full scanner assembly. The peaks at 63.0 kHz and at 95.6 kHz are more difficult to identify, but could correspond to the rotational and vertical mode of the piezotube alone, that the calculations give respectively at 63.7 kHz and 100.0 kHz (from Fig. 3.4). In Fig. 3.6e-f we show the transfer function of the bending modes, measured between +X and -X contacts. The two very small peaks measured at 4.53 kHz and 4.66 kHz correspond to the first order bending modes of the piezotube s_1. The peaks at 26.6 kHz and 27.4 kHz could correspond to the second order bending modes s_2, and the peak at 29.5 kHz to the rotational mode s_3. We do not find correspondence to the calculations for the other small peaks, and the strong peak at 72.1 kHz could correspond to the bending mode of the tip s_5, even if we are doubtful that this could lead to such a sizable response of the piezotube.

The lowest resonant frequencies of the STM head thus correspond to the bending modes of the piezotube and of the STM head, which are substantially less critical for STM measurements than the vertical modes. The walker assembly, often a critical point for the vertical stability, proves to be the stiffest reported to date for a Pan-style head. Taken together, this confirms the exceptional stiffness of our STM head.

3.3 Cryogenic insert

The STM head is mounted at the bottom of a home-built cryogenic insert that operates at the base temperature of 4.27 K. The insert is rigidly connected to the UHV chamber and the table and it is placed in a ^{4}He bath cryostat. The cryostat has a capacity of 65L, which yields a hold time of ≈275 hours (≈11 days).

A picture of the cryogenic insert with the indication of the main parts is shown in Fig. 3.7. The bottom part of the insert, where the STM is rigidly connected without

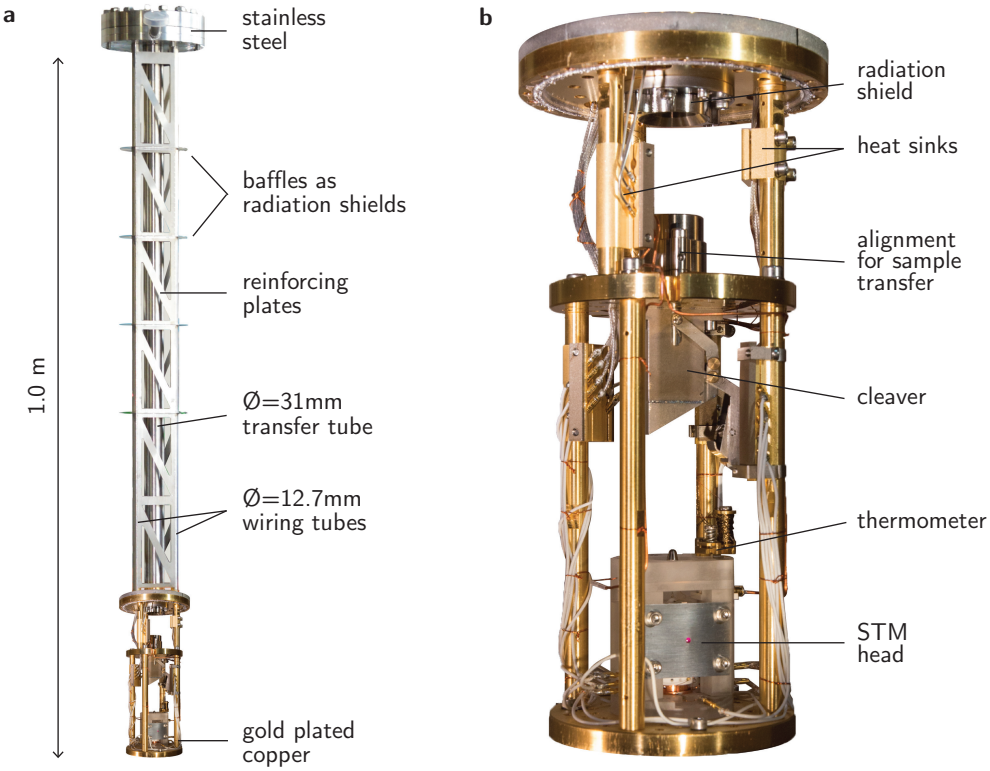

Figure 3.7: **a**, Photograph of the full cryogenic insert without the can that closes the bottom part. **b**, Zoom of the bottom part where the STM is mounted.

the use of springs, is made of gold-plated oxygen-free copper to optimize the thermal connection to the ^{4}He bath. It is enclosed in a gold-plated copper can (not shown in the picture), sealed with an indium wire gasket. The connection to the room temperature UHV chamber is made of thin-walled stainless steel tubes, that are used for pumping and wiring.

The design of the cryogenic insert has also been optimized for maximum stiffness. For this reason, we opted for a reinforced insert structure that features four stainless steel tubes. The central tube has an outer diameter of 31.0 mm and wall thickness of 0.5 mm and it is used as sample transfer line and main pumping line. The three smaller tubes (of outer diameter 12.7 mm and wall thickness 0.25 mm) are used for wiring and are placed in a triangular pattern around the central one. We find that choosing three tubes for wiring, instead of two, drastically improves the stability for the pendulum mode, with the resonant frequency corresponding to this mode increasing by 50%. Furthermore, we provide additional stability by connecting the

tubes with thin (0.3 mm) stainless steel plates. These plates have triangular holes in order to reduce the heat transfer from room temperature to the ^{4}He bath, and are laser spot welded directly to the tubes. Around the tubes, and perpendicular to them, we place four stainless steel baffles that act as radiation shields inside the dewar neck, to reduce the radiation heat transfer to the ^{4}He bath.

All the extra features that we added to improve the stability imply a higher heat conduction to the ^{4}He bath, and a compromise has to be found between stability and desired helium consumption. With our particular design we still obtain an excellent helium consumption of 0.18 L/h (4.3 L/day), which ensures a very quiet helium boil-off noise and allows for >7 days long measurements.

The bottom part of the insert is provided with a radiation shield and a sample cleaving stage. The radiation shield can be placed with the sample transfer mechanism and it significantly reduces by 0.3 K the temperature measured on the STM head. The cleaver is also actuated by the sample transfer mechanism, and it has a bucket that collects the cleaved rods. Before cleaving, the samples are thermalized for a few minutes on the 4 K plate, and we estimate that the cleaving temperature is ≈ 20 K.

3.4 Vibration isolation table

The vibration isolation table is made of two parts: a rigid stainless steel hollow frame with triangular shape and a 40-mm-thick triangular aluminum plate. The plate is rigidly connected to the frame by screws, and the assembly is designed with the specifications of not having any resonant frequencies below 300 Hz. The frame is mounted on top of three negative spring coefficient vibration isolators[6] with resonant frequency 0.5 Hz. In order to reduce acoustic-induced noise and to increase the mass of the table, the frame is filled with lead shots to reach a weight of the total system of ~ 1000 kg. The full system is standing on a measurement island that is decoupled from the surrounding walking floor, but is not additionally isolated with dampers from the foundations.

3.5 UHV chamber

The fully home-built UHV chamber comprises a small load lock chamber and a main preparation chamber. A turbo pump, which is switched off during measurements, is connected to the load lock, and an ion getter pump is installed on the main chamber, leading to a base pressure of $p = 3 \times 10^{-10}$ mbar. Sample storage space and manipu-

[6] Minus K® 800CM-1.

lators are provided in both chambers. In the main chamber, we installed an ion gun for Ar sputtering and a home-built sample heater.

3.6 Performance

We test the performance of our microscope by measuring vibrational noise spectra at the tunnel junction and by obtaining topographic and spectroscopic data on the correlated metal Sr_2RhO_4. Here, we briefly show the data to demonstrate the performance of the microscope, while the physics of Sr_2RhO_4 is discussed in the dedicated chapter 6.

3.6.1 Current and height noise at the tunneling junction

We first characterize the noise level of our laboratory by measuring both vibrations with a seismometer[7] and acoustic noise with a low-frequency microphone[8]. The measurement is reported as linear spectral density (LSD) of the velocity for the vibrations and of the pressure difference for the acoustics. The spectra are obtained by Fourier transforming one minute of real time data with the Welch method using a Hamming window.

We report in Fig. 3.8a typical spectra of (i) the vibrations measured on the island where the table is standing, (ii) the vibrations measured on the table, (iii) the sound measured in the surrounding room. The table reduces the general vibrational noise of about one order of magnitude after 10 Hz, and it dampens many of the peaks. It is instead less effective in reducing the sound-induced noise, as it can be noticed from the peak at 24 Hz that is only partially dampened.

In Fig. 3.8b we show the vibrational noise at the tunnel junction as the linear spectral density of the z height (corresponding to the tip-sample distance) measured in feedback on a $(Pb,Bi)_2Sr_2CuO_{6+x}$ sample at setup condition $V = 300\,mV$ and $I = 150\,pA$. Remarkably, the noise is very low, with an average vibration level of $\approx 6\,fm/\sqrt{Hz}$ and only two peaks with amplitude bigger than $20\,fm/\sqrt{Hz}$, respectively at 12 Hz and 50 Hz.

In Fig. 3.8c we further show the linear spectral density of the current noise measured with the same tunneling junction and setup condition. With tip retracted, we achieve an average noise level of $\approx 8\,fA/\sqrt{Hz}$. The preamplifier we use[9] has a noise floor of $6.5\,fA/\sqrt{Hz}$.

[7] Guralp CMG-40T.
[8] G.R.A.S. 46AF.
[9] FEMTO LCA-4K-1G.

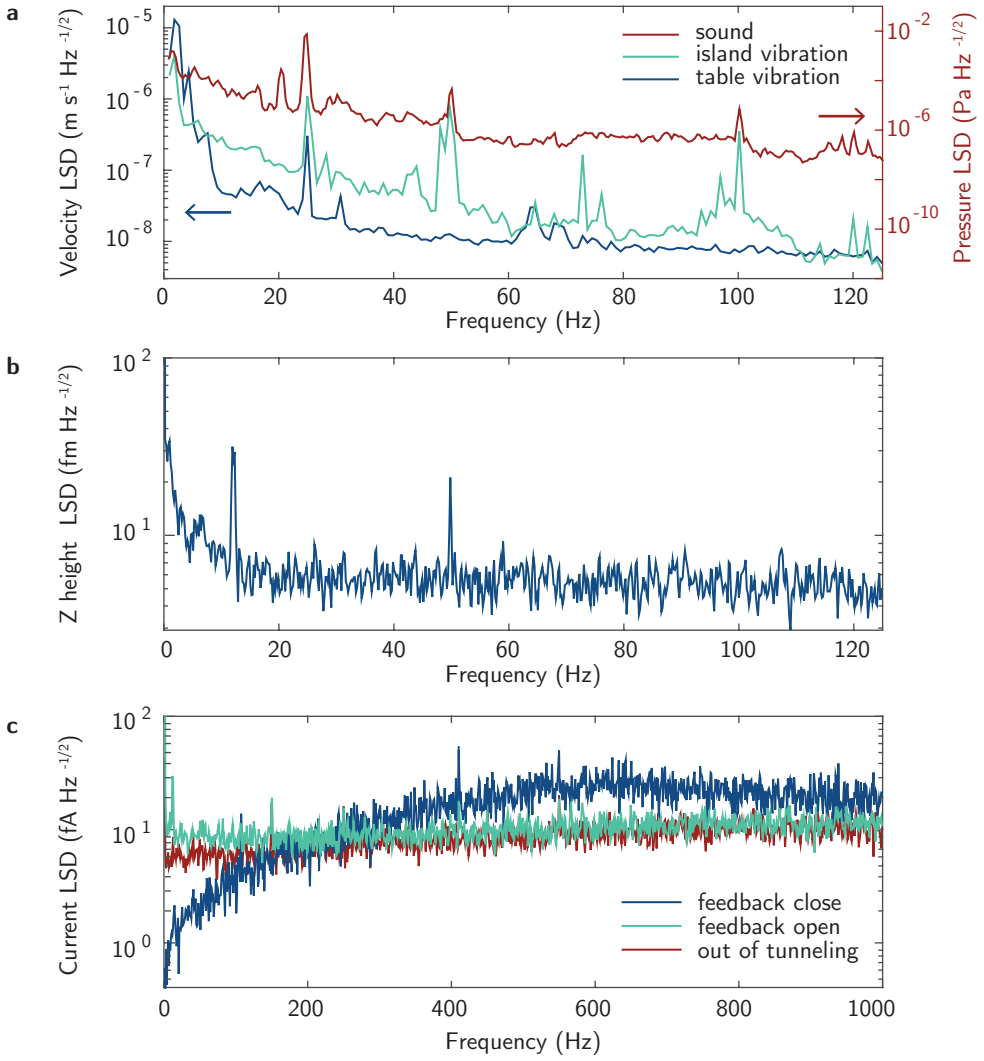

Figure 3.8: **a**, Linear spectral density (LSD) of the velocity measured in the Z direction on the island and on the STM table with a seismometer (Guralp CMG-40T). In the same graph, with scale on the right axis, acoustic noise is reported as LSD of the pressure difference measured with a low-frequency microphone (G.R.A.S. 46AF). **b**, Linear spectral density of the Z height noise at the tunnel junction measured on $(Pb,Bi)_2Sr_2CuO_{6+x}$ at setup condition $V = 300\,mV$ and $I = 150\,pA$. **c**, Linear spectral density of the tunneling current at same tunnel junction as **b**, measured out of tunneling as well as in tunneling with feedback loop closed and open.

In tunneling and with feedback loop closed we can see an increase in the noise to $\approx 20\,\mathrm{fA}/\sqrt{\mathrm{Hz}}$ above 200 Hz, with some peaks reaching up to $\approx 50\,\mathrm{fA}/\sqrt{\mathrm{Hz}}$. The feedback takes care of reducing the low frequency noise.

An important figure of merit for spectroscopic measurements is the out-of-feedback current noise (in tunneling and with feedback loop open). We obtain a noise level of $\approx 10\,\mathrm{fA}/\sqrt{\mathrm{Hz}}$, with only the peaks at 12 Hz and 50 Hz higher than $20\,\mathrm{fA}/\sqrt{\mathrm{Hz}}$, which ensures the capability of performing high quality spectroscopy experiments.

3.6.2 Quasiparticle interference on Sr_2RhO_4

To demonstrate the topographic and spectroscopic capabilities of the microscope, we show quasiparticle interference measurements on the correlated metal Sr_2RhO_4, that is known to have a highly two-dimensional electronic structure [68–70].

The sample is cleaved at the 4 K cleaving stage and immediately transferred to the STM head. Measurements are performed with a chemically etched tungsten tip that has previously been prepared by field emission on a gold surface. Atomic resolution can be easily achieved, as shown in the $15 \times 15\,\mathrm{nm}^2$ topograph in Fig. 3.9a and in the corrugation profile along the black line plotted in Fig. 3.9b. The cleaved surface shows the SrO layer; the Sr atoms are visible on the surface, with interatomic distance distance $a = 3.85\,\text{Å}$. Moreover, we can observe two different types of defects.

In Fig. 3.9c we plot a typical single $\mathrm{d}I/\mathrm{d}V$ spectrum acquired during a spectroscopic map. The spectrum is metallic, and does not show sharp features.

In Fig. 3.9d we show the real space imaging of quasiparticle interference (QPI) in the conductance layer at -20 meV (with respect to the Fermi level), acquired simultaneously to the topograph in Fig. 3.9a. The defects obviously act as scattering centers for the quasiparticles, creating an interference pattern between the standing waves that emphasizes the quantum mechanical wave nature of the quasiparticles.

In Fig. 3.9e we show the Fourier transform of the real-space QPI pattern measured at the Fermi level during a spectroscopic map. The map is acquired on a field of view of $55 \times 55\,\mathrm{nm}^2$ with 288×288 pixels, thus consists of ≈80000 spectra acquired one after the other without the use of feedback to the tip during the spectra acquisition. The Fourier-transformed data is not symmetrized nor processed in any other way, and still shows sharp features with very high signal-to-noise ratio.

A more comprehensive analysis, including a quantitative comparison with ARPES data from Ref. [69], will be discussed in chapter 6.

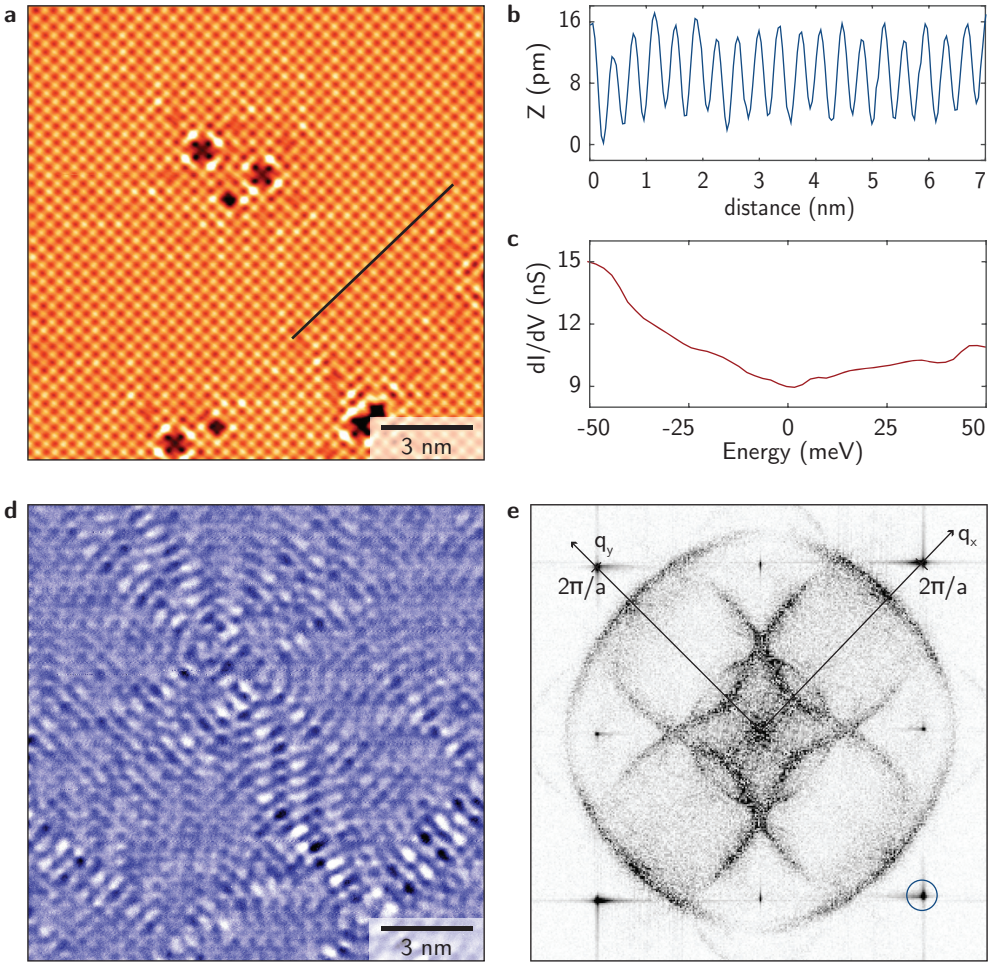

Figure 3.9: STM measurements on Sr_2RhO_4. **a**, Topograph in a field of view of $15\times15\,nm^2$. Setup conditions ($V_b=-20\,mV$, $I_t=600\,pA$). The image is not filtered. **b**, Atomic corrugation profile along the black line in **a**. **c**, Example of a single dI/dV spectrum measured during a spectroscopic map. **d**, Density of states measured simultaneously to the topograph in panel **a**, showing the quasiparticle interference pattern in real space at energy $E=-20\,meV$. **e**, Non-symmetrized Fourier transform of the conductance layer at the Fermi level acquired in a spectroscopic map over a $55\times55\,nm^2$ field of view. One of the Bragg peaks is highlighted in the blue circle.

3.7 Conclusions

In the present chapter, we describe design principles, construction and performance of our ultra-stable STM Dome. We constructed a very stiff microscope by combining smart material choice and design improvement guided by FEA calculations. This allows us to obtain outperforming data quality even in a lab not dedicated to low vibrations, as described in Sec. 3.6. While writing this thesis, the instrument has been moved to a new building with world-class low-vibration facilities, and we believe that this will improve its performance further. In chapter 7, we propose a series of experiments that we are planning to perform with the microscope Dome in the near future.